IEEE Access
Multidisciplinary | Rapid Review | Open Access Journal

Received 10 May 2023, accepted 9 June 2023, date of publication 19 June 2023, date of current version 28 June 2023.

Digital Object Identifier 10.1109/ACCESS.2023.3287486

RESEARCH ARTICLE

Validation of a Compact Microwave Imaging System for Bone Fracture Detection

KESIA C. SANTOS[1,2], (Student Member, IEEE), CARLOS A. FERNANDES[1], (Life Senior Member, IEEE), AND JORGE R. COSTA[1,3], (Senior Member, IEEE)

[1]Instituto de Telecomunicações, Instituto Superior Técnico, 1049-001 Lisbon, Portugal
[2]Instituto Federal da Paraíba, João Pessoa 58015-435, Brazil
[3]Departamento de Ciências e Tecnologias da Informação, Instituto Universitário de Lisboa (ISCTE-IUL), 1649-026 Lisbon, Portugal

Corresponding author: Kesia C. Santos (kesia.farias@ifpb.edu.br)

This work was supported in part by Conselho Nacional de Desenvolvimento Científico e Tecnológico (CNPq), Brazil, under Grant 206841/2014-0; in part by the Fundação para a Ciência e a Tecnologia (FCT) Project PTDC/EEI-TEL/30323/2017 under Grant LISBOA-01-0145-FEDER-030323; and in part by the Fundo Europeu de Desenvolvimento Regional - Portugal 2020 FEDER-PT2020 Partnership Agreement under Grant UID/EEA/50008/2020.

ABSTRACT This work presents a systematic evaluation of the effectiveness of an air-operated microwave imaging (MWI) system for the detection of arbitrarily oriented thin fractures in superficial bones, like the tibia. This includes the proposal of a new compact, portable setup where a single Vivaldi antenna performs a semi-cylindrical scan of the limb. The antenna is operated in monostatic radar mode, near the skin but without contact, thus ensuring hygiene and patient comfort during the exam. The image is reconstructed using a wave-migration algorithm in the frequency domain combined with an adaptative algorithm based on singular value decomposition which removes the skin artifact taking into account the non-uniform bone profile and tissue cover. The study investigates the system resolution, the robustness of the method to the uncertainty of the permittivity and thickness of the involved tested tissues, as well as the robustness to involuntary patient movement. The experimental validation was performed for the first time on an integral *ex-vivo* animal leg, with all tissues present, including skin and fur. It confirmed both the effectiveness of the method, and the feasibility of the setup.

INDEX TERMS Microwave imaging, biomedical imaging, image reconstruction, bones.

I. INTRODUCTION

Nowadays, medical imaging diagnostic is very advanced, providing early and reliable diagnoses, decreasing the mortality rate, and increasing the quality of life of the patients. However, with the increasing rate of requests for radiologic examinations, even with low exposure levels in each exam, there are reasons for caution. In recent studies, it is estimated that low-dose radiation exposure from medical imaging may in the future account for up to 2% of cancers in the USA [1].

Commonly used medical imaging techniques for bone fracture detection and monitoring are radiography scan, computed tomography (CT) scan (both using X-rays), and magnetic resonance imaging (MRI) scan. X-rays are ionizing, and potentially pose health risks [1]. MRI is not ionizing, however it is expensive and time-consuming.

Microwave imaging (MWI) is a nonionizing technique that is growing and increasingly presenting promising results in recent research, to detect breast cancer [2], [3] and [4], brain stroke [5], [6] and [7]. Recently, a portable device was presented to detect breast cancer [8].

The challenges of medical microwave imaging are totally different from microwave imaging in security applications for instance. Body tissues absorb microwaves, limiting their penetration; moreover, the skin reflection is orders of magnitude higher than the faint response from inner tissue contrasts. In the case of bone fractures, the variable thickness of tissues adds to the fracture detection challenge. After massive and promising research, the medical imaging area has been evolving for clinical application. Only in 2019, the MARIA

The associate editor coordinating the review of this manuscript and approving it for publication was Yi Zhang.

MWI clinical system was installed in hospitals in Germany for breast scanning [9].

There are research teams evaluating the feasibility of medical diagnostics using MWI specifically for bone lesions and fractures. In [10], the authors reconstructed bone profiles immersed in a coupling medium. This approach is unattractive for practical applications and complicates the setup. In [11] and [12] the authors use an adapted free space setup, based on a previous clinical prototype Mammowave [13], to detect longitudinal bone fractures and lesions using a 3D tube model. The experimental setup is fixed and bulky, otherwise used for MW breast scan, and not so practical to use with a leg in a clinical scenario. The diameter of the used cortical bone phantom is 11 cm, the marrow diameter is 7 cm, and the longitudinal lesion has 7 mm radius. These unrealistic dimensions may affect the generalization of the results for a real case. In all the previous works, a regular and uniform phantom was used.

In [14] and [15] a portable setup is presented for detecting knee tears, although not being applied for detecting bone fractures. In the proposed setup, the examination is performed with the phantom in a standing posture, without using immobilization. This may be problematic because the proposed MWI reconstruction is based on limb symmetry, which may require precise antenna positioning. It also requires limbs symmetry.

Recently, we proposed in [16] and [17] a MWI-based method for detection of very thin fractures in superficial bones, like the tibia. It was developed for contactless operation, without the need for any coupling medium. The antenna scan was performed along a parallel line to the bone axis, aiming at the detection of thin transversal fractures. The experimental validation was done with 3D-printed cylindrical phantoms, and with *ex vivo* animal bones stripped of tissues.

In the present paper we expand that study to detect arbitrarily oriented thin fractures, namely double transversal and oblique ones. This requires extending the scan from one line to a cylindrical surface and adapting the previous algorithms to deal with the non-uniform distance of the antenna to the bone and the skin artifact. We also evolve the low-cost setup presented in [17] to introduce scanning over a cylindrical surface semi-encircling the leg. The setup is conceived such that the patient may be sitting or in supine posture, and it is the setup, not the patient that needs to be positioned. The longitudinal scan for fixed angular planes is automatic, but at the current stage of development, the angular planes are set manually. In the future all movements of the antenna support can be made automatic.

The most important outcome of this study is that a successful test was made with a fractured integral *ex-vivo* animal limb, without removing any tissue layer, or even the fur. The result showed a clear positive identification of the fracture, demonstrating the effectiveness of the proposed concept and of the dedicated algorithms developed for the inverse scattering problem and image reconstruction. The simplicity of the proposed compact portable system makes it attractive for future use in first-response screening in ambulances, retirement houses, school infirmaries, football fields, veterinary clinics, farms, or low-income settings.

II. SYSTEM DESCRIPTION

The proposed microwave radar-based fracture detection system comprises an antenna capable of spatial scanning around the limb under test, a vector network analyzer to acquire the $s_{11}\,(P_a, f_l)$ scattering parameter at the antenna port as function of the position $P_a(x_q, \theta_h)$ and frequency f_l. A PC is used to control the measurement setup, run the procedures to calibrate the acquired signals, run the dedicated image inversion algorithms, and present the image reconstruction results (see Fig. 1). The details are described next.

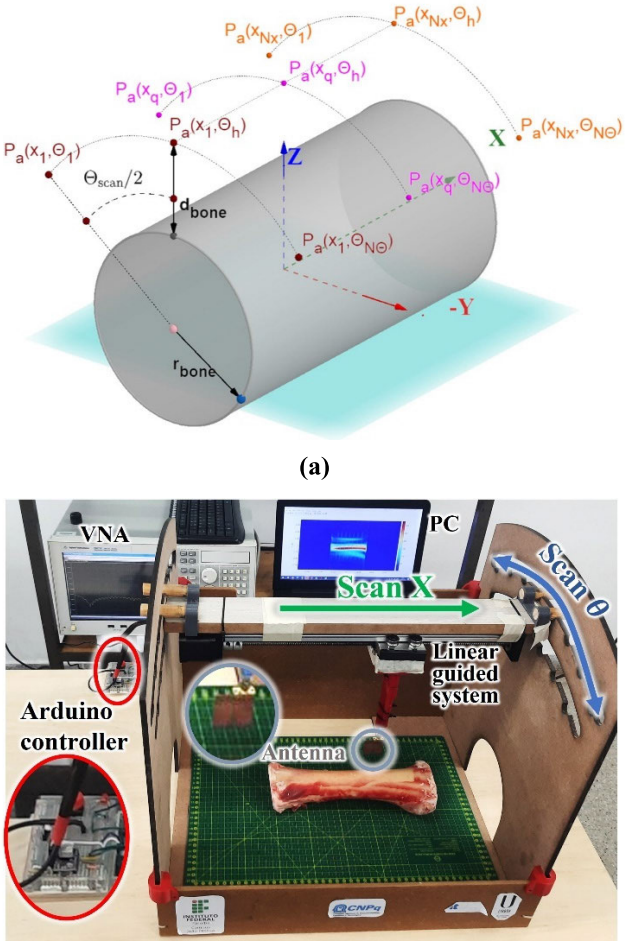

FIGURE 1. MWI system geometry, (a) bone section with the indication of the antenna scan range, and (b) overview of the developed microwave imaging device.

A. MICROWAVE DETECTION SYSTEM

Unlike several MWI systems that report the use of immersion liquid to minimize wave reflections at the skin [10], this setup is contactless, requiring no coupling liquids for maximum hygiene and simplest operation in the field. This air operated

approach is challenging, but it has been shown to be feasible and preferable [4], [16].

Our MWI setup works in monostatic radar configuration. The antenna scans the limb along a cylindrical grid around the bone thus favoring the detection and location of different types of fractures, such as oblique, transversal, and double transversal. The cylindrical grid radius is $r_{ant} = d_{bone} + r_{bone}$, respectively the distance of the antenna tip to the bone surface and the bone radius. The θ_h angle is defined between the zx-plane and the measurement radial plane, with positive values along positive y-axis direction, as shown in Fig. 1(a).

A single Vivaldi antenna acquires the antenna input reflection coefficient $s_{11}(P_a, f_l)$ at each position P_a of the cylindrical grid shown in Fig. 1(a), for all f_l frequencies with $l = 1 \ldots N_f$, within a given broad range. In Cartesian coordinates, this corresponds to $P_a\left(x_q, \theta_h\right) = (x_q, y = r_{ant} \sin(\theta_h), z = r_{ant} \cos(\theta_h))$, where $r_{ant} = r_{bone} + d_{bone}$. The total set of measurements is represented as $\boldsymbol{s_{11}}\left(\boldsymbol{P_a}\right)$, where $\boldsymbol{P_a}\left(\boldsymbol{x}, \boldsymbol{\theta}\right)$ with $\boldsymbol{x} = \left[x_1 \ldots x_q \ldots x_{Nx}\right]$ and $\boldsymbol{\theta} = [\theta_1 \ldots \theta_h \ldots \theta_{N\theta}]$, represent the scanning grid points.

For each θ_h-angle, the single antenna translates longitudinally acquiring the signal at each x_q position, with the help of a linear guided system, using a precision lead screw connected to a NEMA 17 motor, as shown in Fig. 1(b). Distance d_{bone} form the tip of the antenna to the bone surface is much smaller than the wavelength, in the order of 10 mm, to benefit from the better resolution associated with the antenna reactive field.

The system is controlled via an Arduino Uno that is connected to the laptop and to the linear guided system using an USB interface. The antenna is connected to an Agilent E5071C Vector Network Analyzer (VNA) using RF cables to collect the backscattered signals ($\boldsymbol{s_{11}}$). The application for signal processing and image algorithm is coded in MATLAB and runs on a laptop.

B. ANTENNA

Medical imaging requires high resolution, which requires the smallest possible wavelengths. However, microwaves lose penetration depth with increasing frequency. Given that this work is intended for superficial bones, a reasonable compromise between penetration depth, and image resolution is obtained for the 8.3-11.1 GHz frequency interval.

We use a Vivaldi antenna operating in this frequency band. with dimensions 28.0 mm × 29.1 mm × 1.5 mm, as shown in Fig. 2. This antenna was designed to be compact, present a wideband impedance match, and stable near-field distribution with frequency, as required for medical imaging [16]. We highlight that this antenna is compact, mainly for systems operating in air [4], [14].

Fig. 3 shows the result of the full-wave simulation of the antenna s_{11} in free space. The spatial distribution of the amplitude and phase of the E-field is presented in Fig. 4. for the antenna reactive region. The E-field magnitude is reasonably well confined in the forward region of the antenna, with negligible back radiation as desired. The phase plot shows

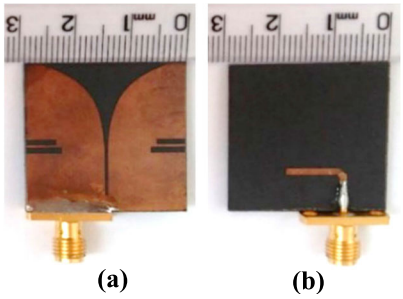

FIGURE 2. Vivaldi Antenna prototype for this application, near a metric ruler (a) front; (b) back.

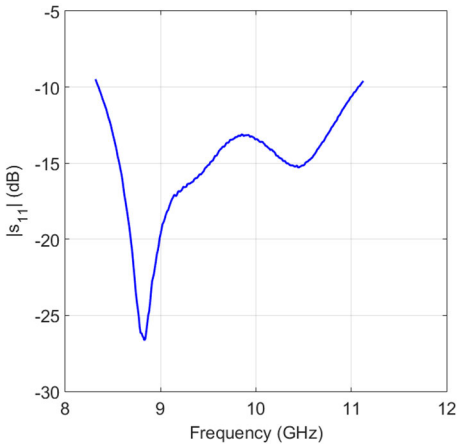

FIGURE 3. Measured reflection coefficient of the antenna in free space.

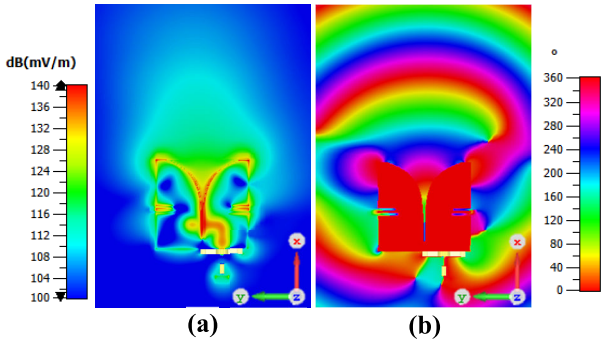

FIGURE 4. Spatial distribution of the y-component of the E-field of the designed Vivaldi antenna prototype, calculated in the reactive region at 9 GHz (a) magnitude; (b) phase.

the formation of an almost spherical wave, right from the reactive-field region, allowing the identification of a phase-center-like point. These amplitude and phase characteristics are maintained over the frequency band (not shown), making this a very appropriate antenna for the imaging setup.

C. IMAGING ALGORITMH

Studies involving real bones, in contactless microwave measurements, present some challenges related to the strong reflection at the air-skin boundary, aggravated by the unknown variation of the bone diameter, skin thickness and texture, along x. These features originate unwanted

contributions to the acquired backscattered $\boldsymbol{s_{11}}(\boldsymbol{x},\boldsymbol{\theta},\boldsymbol{f})$ signals, which can mask the much weaker response from the fracture.

To remove these unwanted signals, some pre-processing is necessary on $\boldsymbol{s_{11}}(\boldsymbol{x},\boldsymbol{\theta},\boldsymbol{f})$. In this work, we first apply a regional average filter (RAF) to the signal. Considering the non-uniform shape of the target, we divide the $\boldsymbol{x}$ set into B non-overlapping sub-regions $\boldsymbol{x} = [\boldsymbol{x}_{R1} \ldots \boldsymbol{x}_{Rb} \ldots \boldsymbol{x}_{RB}]$, where the backscattered signals are more likely to be considered locally similar. Each sub-region has the same number of positions, e.g., $\boldsymbol{x}_{R1} = \{x_1, x_2, x_{N_x/B}\}$. The RAF is applied to each backscattered signal in the regional subset by subtracting from it the regional average signal calculated over the x-dimension,

$$\boldsymbol{s_{11}}^{\boldsymbol{cal}}_{R_b}\left(\boldsymbol{x}_{R_b},\theta_h,f_l\right) = \boldsymbol{s_{11}}_{R_b}\left(\boldsymbol{x}_{R_b},\theta_h,f_l\right) - \overline{\boldsymbol{s_{11}}_{R_b}\left(\boldsymbol{x}_{R_b},\theta_h,f_l\right)} \tag{1}$$

The filtered signal of the full set is then obtained by concatenating each regional subset as $\boldsymbol{s_{11}^{cal}} = \left[\boldsymbol{s_{11}}^{\boldsymbol{cal}}_{R_1} \ldots \boldsymbol{s_{11}}^{\boldsymbol{cal}}_{R_b} \ldots \boldsymbol{s_{11}}^{\boldsymbol{cal}}_{R_B}\right]$.

The unwanted signals that persist after (1), may still create artifacts in the reconstructed image. In this step, it is common to use an artifact removal algorithm to separate the wanted from the unwanted contributions [3], [18], [19] and [20].

In our work, we used an algorithm based on Singular Value Decomposition (SVD) [21], [22], and [23] for the skin artifact removal. It allows separating the stronger response of the non-uniform bone surface and skin, from the weak bone fracture response. The SVD is described by

$$\boldsymbol{s_{11}^{cal}}(P_a,f_l) = U\Sigma V^H = \sum_{k=1}^{N}\sigma_k u_k v_k^H \tag{2}$$

in which U is the unitary matrix of left singular values, V^H is the Hermitian of the unitary matrix of right singular values, and Σ represents a square diagonal matrix composed of the singular values σ_k of $\boldsymbol{s_{11}^{cal}}(P_a,f_l)$ ordered in decreasing amplitude sequence. The maximum value of k is the rank of the matrix $\boldsymbol{s_{11}^{cal}}(P_a,f_l)$.

The filtered signal is obtained by removing the strongest $(k < g)$ singular values from the signal, which are responsible for the artifacts

$$\boldsymbol{s_{11}^{s}}(P_a,f_l) = \sum_{k=g}^{N}\sigma_k u_k v_k^H \tag{3}$$

Parameter g is determined after proper analysis of a set of representative examples of the tested scenarios.

Direct use of this process for all data, for instance as in [23], works better for uniform shapes. It may not be so effective for non-uniform shapes, where its effect may still overshadow the response of the fracture. In order to mitigate the effect of non-uniformities, an adaptive SVD approach was used by the authors in [4] for breast cancer detection, and in [16] for bone fractures detection. In the present work we also implement an adaptative SVD process: the scanned area $s_{11}^{cal}(P_a,f_l)$, is divided into Q subregions, each one with Na/Q elements, in which the backscattered signal can be considered locally similar. The number of these Q subregions is not necessarily equal to the number of B subregions of the previous step.

$$\begin{aligned}\boldsymbol{s_{11}^{cal}}(P_a,f_l) = [&\boldsymbol{s_{11}^{cal}}(x_{\mathrm{R1}},\theta_h,f_l)\\ &\ldots \boldsymbol{s_{11}^{cal}}\left(x_{\mathrm{Rq}},\theta_h,f_l\right)\\ &\ldots \boldsymbol{s_{11}^{cal}}\left(x_{\mathrm{RQ}},\theta_h,f_l\right)]\end{aligned} \tag{4}$$

Equations (2) and (3) are then applied to each subregion of $\boldsymbol{s_{11}^{cal}}(P_a,f_l)$. All the subregion vectors are non-overlapping and contain the same number of antenna positions. In each subregion, the same number of singular values are removed. Eq (4) is the SVD filtered response, g is applied according to each scenario.

The subsequent step is to concatenate the subregion results into a vector $\boldsymbol{s_{11}^{s}}(P_a,f_l)$. This signal is free from spurious scattering and denotes the complete set of values for all N_f frequencies.

The reconstructed image is based on wave migration [24], obtained from

$$I_{mn} = \frac{1}{N_f^2 N_a^2}\left|\sum_{l=1}^{N_f}\sum_{i=1}^{N_a}\boldsymbol{s_{11}^{s}}\left(P_{a_i},f_l\right)e^{j2k_0 D_{i(m,n)}}\right|^2 \tag{5}$$

with the straight path distance between the measurement point and test point on the limb pixel $D_{i(m,n)} = d_0 + \sqrt{\varepsilon_{r_{av}}}d_1$, in which d_0 and d_1 are travelled lengths in air and tissues, respectively.

At each test pixel where a target (fracture) exists, the sums in (5) add up coherently, increasing its value with P_{a_i} and N_f. Otherwise, the signals add-up incoherently, and the sum tends to zero. In I_{mn} the frequencies are summed, considering the contributions of all antenna positions $\boldsymbol{P_a}(\boldsymbol{x},\boldsymbol{\theta})$ and frequencies to the (m, n) pixel.

In practical situations, it is not possible to know exactly the permittivity values of each patient's tissues. Therefore, an average tissue permittivity, $\varepsilon_{r_{av}}$ is estimated following [14], where we consider an estimated thickness of each tissue.

$$\varepsilon_{r_{av}} = \frac{\sum_{j=1}^{N_T} t_j \varepsilon_{rj}}{t_{total}} \tag{6}$$

where ε_{r_j} represents the dielectric constant of each tissue, t_j its thickness, t_{total} the total thickness of the tissues in the phantom section, N_T the total number of tissues, and $j$the index of the tissue.

The thickness of each animal tissue was obtained experimentally. The measurements were taken in a transversal section of the fracture, and are shown in Table 1. The values of the dielectric properties were obtained in [25].

When available, it is possible to use online image databases to better estimate the human tissue thickness, as mentioned in [14], [26], and [27]. We discuss ahead the sensitivity of the imaging process to the expected uncertainty in these values.

TABLE 1. Tissue dimensions and permittivity.

		Ovine	Goat	ε_{r_j}
t_j	*Skin*	No skin	2-mm	32.2
	Tendon	4-mm	5-mm	30.9
	Muscle	4-mm	2-mm	44.7
	Bone	12-mm	11-mm	8.4
$\varepsilon_{r_{av}}$		20.19	20.07	---

We use a performance indicator to quantify the quality of the image reconstruction algorithm: signal-to-clutter ratio (SCR) [2]. SCR is defined as the ratio between the maximum intensity corresponding to response in the fracture region, S, and the maximum intensity of the background clutter, C, within the scanned region.

III. SIMULATIONS RESULTS

This section focuses on four main aspects, A) minimum detectable fracture thickness; B) tolerance to permittivity uncertainty; C) resolving power of the imaging system (resolution); D) detection of oblique fractures. We also test the robustness of the imaging process to limb position errors due to involuntary patient movement.

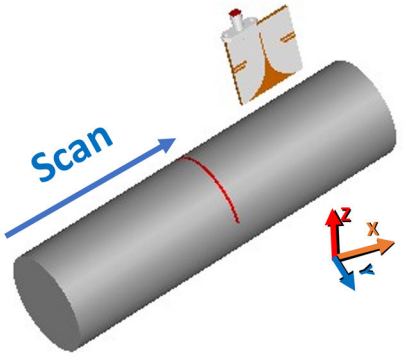

FIGURE 5. Numerical phantom with transversal fracture.

Full-wave simulations are preformed using CST Microwave Studio [28]. We consider a simplified numerical model of the tibia [16], represented by a uniform 40 mm diameter, 150 mm long cylindrical phantom (see Fig. 5), with the dielectric properties of cortical bone $\varepsilon_r = 8.4$ (except where mentioned otherwise). The fracture is represented by different thickness discs, with dielectric properties of blood. The dielectric properties of all tissues are found in [26]. Previous studies [17] and the results in later sections of this paper show that simulation results for this model compare well with our measured results in biological bones.

As mentioned in a previous work [16], even if more elaborate phantoms can be analyzed, these simpler ones already describe the main features of the response, enabling to conclude about the detection feasibility.

The antenna is oriented such that the E-field is parallel to the bone axis. For each θ_h plane, out of seven planes in the $[-24° < \theta_h < 24°]$ interval (see Fig. 1(a)), the antenna performs a linear scan along x, stopping at $N_x = 41$ positions in the $[-40 < x_q < 40]$ mm interval, where the s_{11} at the antenna port is calculated for $N_f = 201$ frequencies. The nominal distance between the antenna tip and the bone boundary is $d_{bone} = 10\ mm$.

Analysis of simulations for different scenarios showed that that a reasonable number of subregions for the regional average is B = 3. The same is used for the adaptive SVD, that is, Q = 3. This allows to cope with the increase of bone diameter towards the bone ends, compared to the mid region. In general, the number of removed singular values is $g = 2$ in the region of the bone ends, and $g = 1$ in the mid region.

A. DETECTABLE FRACTURE THICKNESS

We investigate the capability of the system to detect and locate thin fractures. In optical systems, the image resolution is diffraction limited to $\lambda_m/2$, where λ_m is the wavelength in the medium with ε_r permittivity. In our case, this would correspond to about 10 mm, at mid-band.

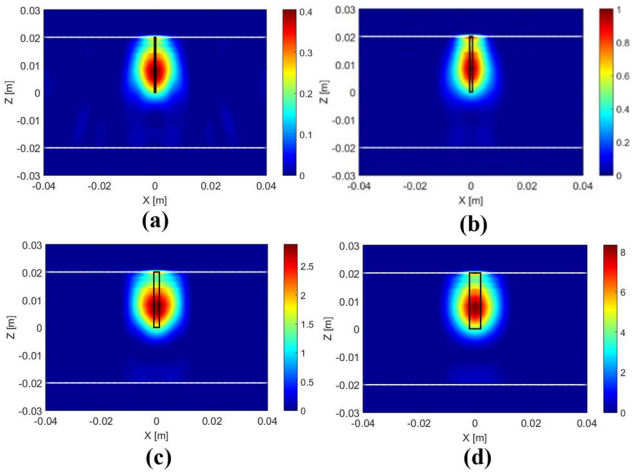

FIGURE 6. Reconstructed images from numerical tibia phantom with a transversal fracture (a) 0.5 mm thick; (b) 1 mm tick; (c) 2 mm tick and (d) 4 mm tick. The white lines define the bone boundary. The position and thickness of the fracture in the numerical model are indicated by the dotted black line.

In this study, we test transversal fractures with 0.5-mm, 1-mm, 2-mm, and 4-mm thicknesses, which are narrower than the resolution limit, but relevant cases in the context of the practical application. The corresponding image calculated using Eq. (5), is shown in Fig. 6. It is a map of the reflected intensity, where the dotted black line indicates the position and thickness of the fracture in the numerical model, and the white lines indicate the bone boundary. The result shows that all tested fracture thicknesses produce an identifiable response, although with smaller amplitudes as the thickness decreases. Its effective detectability in a more complex scenario will depend on the relative strength of this response compared to possible artifacts in that scenario. As expected, according to the theorical resolution limit, the width of the detection spot in the image remains in the order

of 10 mm for all these cases, preventing the determination of the actual fracture thickness. As a conclusion, subwavelength fracture thicknesses produce a response that may allow the identification of its location, but not its thickness.

B. TOLERANCE TO PERMITTIVITY UNCERTAINTY

We instigate the impact of permittivity value uncertainty on image reconstruction. This verification is relevant because, in a real exam, it is not possible to determine the exact values of the parameters that appear in eq. (6).

We consider, as an example, a scenario where the permittivity value used in the inversion algorithm matches the nominal permittivity value of the phantom (cortical bone) $\varepsilon_r = 8.4$. This result in presented in Fig. 6 (b). We compare it with the cases where the permittivity used in the image reconstruction deviates from this nominal value by $\pm 10\%$ and by $\pm 40\%$. Results in Fig. 7 and Table 2 show that the fracture is detected in any case at its true position, although with slight variation of the maximum intensity, but with SCR almost unchanged within the $\pm 10\%$ interval, and reduced by only 1.9 dB for $\pm 40\%$ deviation with respect to nominal. This degradation is negligible and the identification remains clear, confirming the required robustness of the image inversion algorithm with respect to permittivity uncertainty.

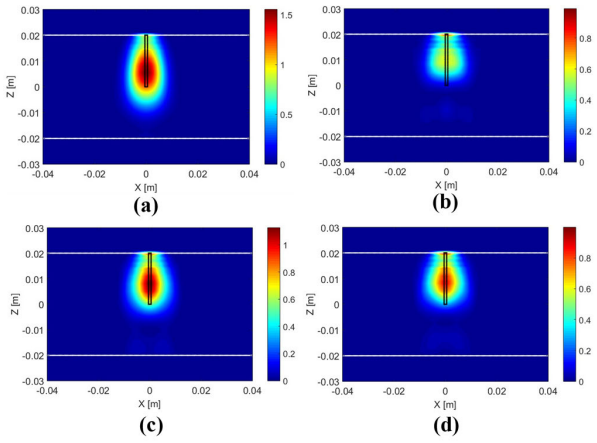

FIGURE 7. Reconstructed images from numerical tibia phantom with transversal fracture at the slice y = 0 mm (a), $\varepsilon_r = -40\%$, (b) $\varepsilon_r = +40\%$, (c) $\varepsilon_r = -10\%$, and (d) $\varepsilon_r = +10\%$. The white lines define the bone boundary. The actual position and thickness of the fracture in the numerical model are indicated by the black line.

TABLE 2. SCR for uncertain knowledge of permittivity.

ε_r	SCR (dB)
$\Delta\varepsilon_r = -40\%$	8.2
$\Delta\varepsilon_r = -10\%$	9.2
$\varepsilon_r = 8.4$	9.4
$\Delta\varepsilon_r = +10\%$	9.0
$\Delta\varepsilon_r = +40\%$	7.5

C. RESOLVING POWER OF THE IMAGING SYSTEM

Still related to system resolution, it is relevant to determine the capability of the imaging system to distinguish between two close fractures. This gives a measure of the resolving power of the imaging system, and it is relevant e.g. in clinical situations involving multiples lesions.

Different authors analyze resolution in microwave imaging of the breast and of the lungs [8], [29], [30], [31], [32], and [33]. In these studies, the targets are PEC or dielectric cylinders, with radius ranging from 5 mm to a few cm, separated by distances of the order of 50 mm. These authors report the appearance of coupling effects that may limit the separability of the targets in the image. They resolve two contiguous targets down to a distance of 40 mm between them.

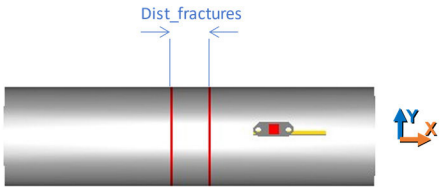

FIGURE 8. Numerical phantom with double transversal fracture. The considered distance between fractures is either 10 mm or 15 mm.

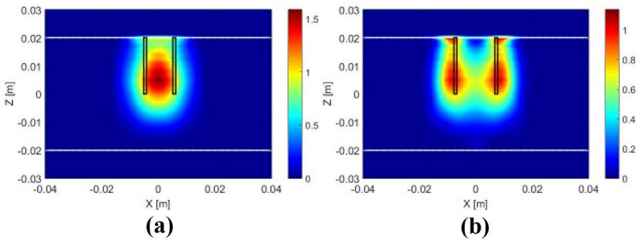

FIGURE 9. Reconstructed image at the y = 0-mm plane of two contiguous bone fractures with (a) 10 mm separation; (b) 15 mm separation. The white lines define the bone boundary. The actual position and thickness of the fractures are indicated in the numerical model by the black line. Bone permittivity is $\varepsilon_r = 8.4$.

In our work, the targets are 1-mm thick transversal bone fractures, with much smaller separation, of 10 mm and 15 mm, as shown in Fig. 8. The results are presented in Fig. 9 (a) for 10-mm separation and in Fig. 9 (b) for 15 mm separation. The computed metric value is SCR = 4.5 dB. Indeed, for the 10-mm case, the proximity of the two fractures creates an overlap of their responses in the reconstructed image that prevents a neat separation of their images. However, for the 15-mm distance case, the fractures' image already separate well.

For the 15-mm separation, we also evaluate how patients' involuntary movement during an examination may impact this result, since movement is a critical factor in medical image quality. For that, we change the distance d_{bone} in some of the seven θ_{scan} planes scanned in the same exam. We consider two cases: in case 1), we make $d_{bone} = [10, 5, 10, 5, 10, 5, 10]$ mm in the consecutive θ_{scan} planes, and the result is shown in Fig. 10 (a) with SCR = 3.8 dB. For case 2), we make $d_{bone} = [10, 15, 10, 15, 10, 15, 10]$ mm, and the result is shown in Fig. 10 (b) with SCR = 4 dB. Comparison with the nominal case of Fig. 9 (b),

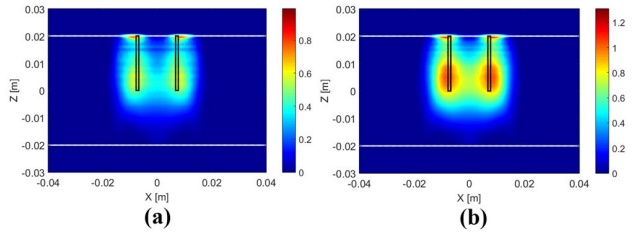

FIGURE 10. Reconstructed image at the y = 0-mm plane of two contiguous bone fractures with 15 mm separation; (a) with altered d_{bone} (case 1); and (b) with altered d_{bone} (case 2). The white lines define the bone boundary. The actual position and thickness of the fractures are indicated in the numerical model by the black line. Bone permittivity is $\varepsilon_r = 8.4$.

where $d_{bone} = 10$ mm for all θ_{scan} planes, allows to conclude that the fractures are still resolvable despite the simulated target movement during the exam.

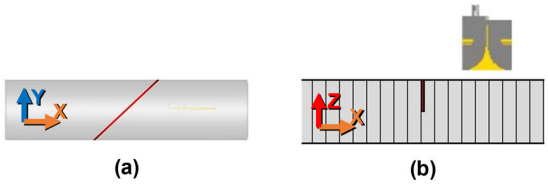

FIGURE 11. Numerical phantom with 45° oblique fracture, a) yx plane (b) xz plane cut view at y = 0.

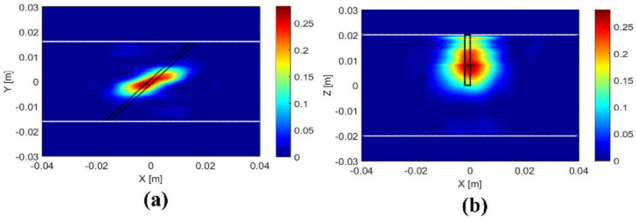

FIGURE 12. Reconstructed image of an oblique fracture in the (a) $z = 10$ *mm* slice and (b) $y = 0$ plane with nominal distances. The white lines define the bone boundary. The actual position and thickness of the fracture in the numerical model are indicated by the dotted black line. Bone permittivity is $\varepsilon_r = 8.4$.

D. DETECTION OF OBLIQUE FRACTURES

In this section, we present results obtained for oblique fractures, aligned at 45° angle with respect to the x-axis, as shown in the Fig. 11.

The results in Fig. 12 (a)-(b), still show the fracture detection, with an inclined response, although not exactly with the same tilt as the fracture. The metric value is SCR = 6.37 dB, which indicates good detection.

In this case we also evaluate the influence of patient's involuntary movement during the examination, considering the same d_{bone} variation approach used in the previous example. The results for case 1) are shown in Fig. 13 (a)-(b) with SCR = 6.1 dB, and case 2) are shown in Fig. 13 (c)-(d) with SCR = 6 dB, respectively. There is a slight increase of the artifacts and decrease of the amplitude, but the fracture is still detectable. This demonstrates the robustness of the detection to different conditions that are expected in a realistic scenario.

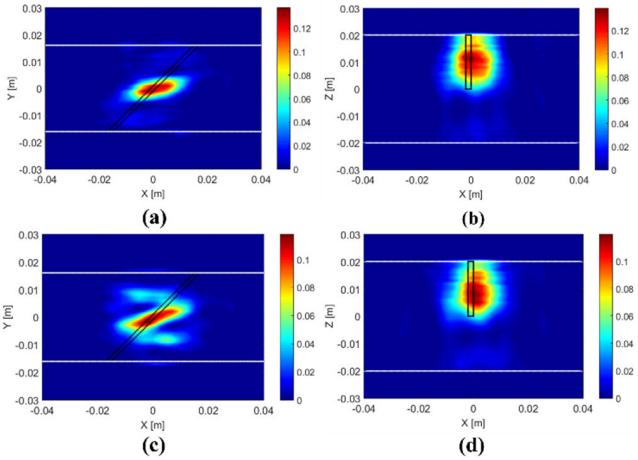

FIGURE 13. Reconstructed image in an oblique fracture in the $z = 10$ *mm* slice (left column) and $y = 0$ plane (right column). (a)-(b) intentional positioning error case 1; and (c)-(d) case 2. Permittivity is $\varepsilon_r = 8.4$. The white lines define the bone boundary. The actual position and thickness of the fracture in the numerical model are indicated by the dotted black line.

IV. EXPERIMENTAL RESULTS

To validate the effectiveness of our system for detection of arbitrary fractures in superficial bones, four distinct *ex-vivo* phantoms were used. In all cases the fresh animal tissues were obtained from the local consumer market, kept refrigerated and hydrated until the measurement. In Section IV-A and B we introduce fractures in bovine bones, in Section IV-C we use an ovine leg and in Section IV-D a goat leg is used with all tissues present, including the skin and fur.

The $\boldsymbol{s_{11}}\left(x_q, \theta_h, f_l\right)$ was acquired in this experiment for $N_x = 41$ points in the $[-40 < x_q < 40]$ mm interval for successive $N_\theta = 7$ angular positions with angular positions with $[-24^\circ < \theta_h < 24^\circ]$ at every 8°, $N_f = 201$ frequency points. The tip of the antenna was positioned at $d_{bone} = 15$ mm away from the boundary bone, at its mid length along x. The fractured tibia was aligned and measured. The antenna was fed with 10 dBm signal level. The values of B, Q and g used in the inversion algorithm are indicated in the each of the following sections.

A. DOUBLE TRANSVERSAL FRACTURES

In the first test we used an *ex-vivo* stripped bovine tibia bone, with 40-mm minimum diameter and 150-mm length. We tested experimentally the capability of the system to detect and locate two closely spaced bone fractures. Two cuts were opened on the surface of the bovine bone about 15 mm apart from each other, about 1-mm thick and 20-mm deep, as shown is Fig. 14. The fractured tibia was carefully aligned in the setup before measurement.

The corresponding results in Fig. 15 were calculated considering $B = 3$, $Q = 3$ and $g = 1$ for the central region of the bone and $g = 1$ for the edge regions, and a permittivity $\varepsilon_r = 8.4$ [25]. The image clearly shows two well separated fractures, in the correct position. In these measured results, the cross-coupling effect between the fractures seems to be

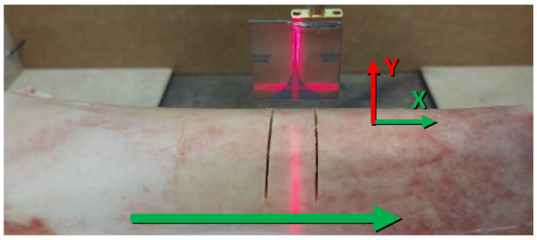

FIGURE 14. Experimental setup showing two transversal fractures opened in a bovine tibia, in the *yx*-plane, with $\lambda/2$ distance between fractures.

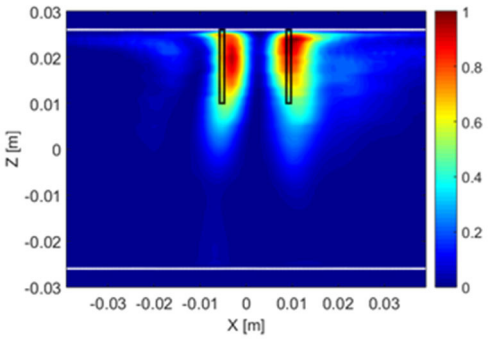

FIGURE 15. Reconstructed images from *ex-vivo* bovine tibia with a double transversal fracture (a) at the slice $z = 15$ *mm*, (b) at the plane $y = 0$ mm, with $\varepsilon_r = 8.4$. The white lines define the bone boundary.

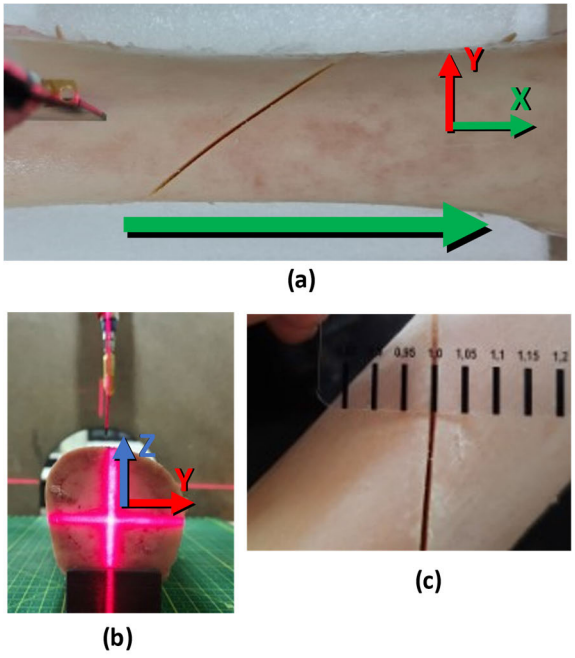

FIGURE 16. Experimental setup showing an oblique fracture in bovine tibia bone in (a) yx-plane, (b) zx-plane, and (c) fracture thickness compared to a gauge.

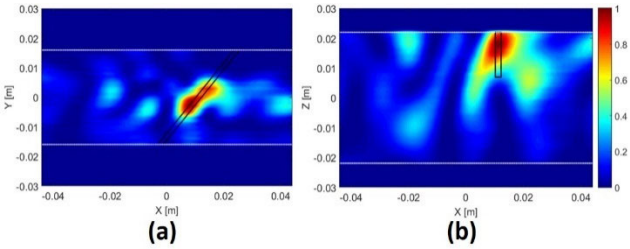

FIGURE 17. Reconstructed images from ex-vivo bovine tibia with an oblique fracture (a) at the slice $z = 15$ *mm*, (b) at the plane y = 0 mm, with $\varepsilon_r = 8.4$. The white lines define the bone boundary.

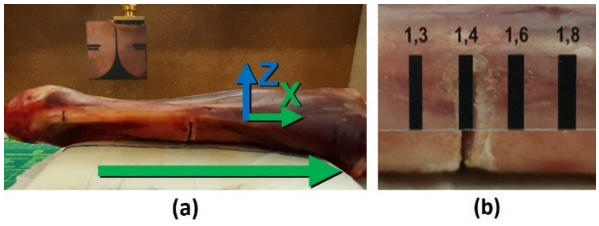

FIGURE 18. Experimental setup (a) Ovine leg with transversal fracture (b) size of the fracture (1.4 mm).

lower than predicted by simulations, confirmed by SCR = 5.8 dB. In the general rule can be established with this respect, but this experimental result is enough to confirm that these thin fractures can be detected in biological bones, reinforcing the robustness of the proposed image inversion methods.

B. OBLIQUE FRACTURES

For this first test we also used an *ex-vivo* stripped bovine tibia bone, with 40-mm minimum diameter and 150-mm length. An oblique cut, with 50° inclination relative to the x-axis was opened in the mid region of the animal bone, about 1-mm thick and 15-mm deep, as shown is Fig. 16.

Fig. 17 (a)-(b) shows the corresponding reconstructed image. The image was reconstructed considering permittivity $\varepsilon_r = 8.4$, $B = 3$, $Q = 3$ and $g = 1$ for the central region of the bone and $g = 1$ for the edge regions. The dotted black line indicates the fracture position. The detection of the fracture is clear, allowing to identify its inclination in the xy-plane.

It is possible to observe in the zx-plane (Fig. 17 (b)), that the system could detect the fracture depth along z, although with some image artifacts. In fact, the image depth of field along the y-axis is not narrow enough to prevent the projection of the fracture length from appearing also in the $y = 0$ plane, as can be confirmed in Fig 17 (a). The metric value for this image is SCR = 5.65 dB, which indicates good detection.

C. TRANSVERSAL FRACTURE IN OVINE LEG WITHOUT SKIN

We significantly evolved our study by using fresh animal limbs, with integral flesh, obtained from a local supplier. We used an ovine leg, with all the tissues present, except the skin, as shown in Fig. 18 (a).

The bone was carefully sectioned, preserving tendon, nerves, and muscle in the scanning area. The fractured leg was then positioned and aligned in the setup, with the incised bone at the bottom. The antenna scanned the region above the intact tissues of the leg, as shown in Fig. 18 (a). The leg cross-section was of course not axis symmetrical; the tibia was located for negative y and z, closer to the muscle-air interface.

Considering that this shape was cluttered with muscles, we measured the scattered fields just in 3 planes, $\theta_h = [-8°, 0°, 8°]$, within the $[-30 < x_q < 30]$ interval, and with $d_{bone} = 16$ mm measured at its mid length along x. The total scanning time was 6 minutes and the computational time to process all measurements was 1.5 minutes.

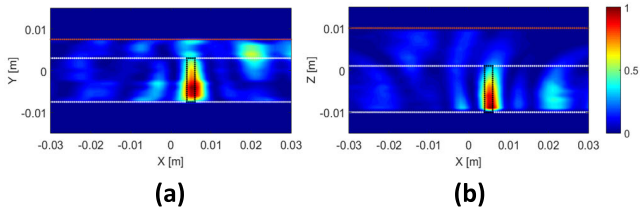

FIGURE 19. Reconstructed images from ex-vivo ovine leg transversal fracture (a) at the slice at $z = -6$ *mm*, and (b) at the slice at $y = 0$ mm, with $\varepsilon_{r_{av}} = 20.19$. The white lines define the bone boundary, and the brown line the soft tissues boundary.

The results are shown in Fig. 19 (a) and (b), which include muscle, tendon and bone regions, the latter delimited with the white lines. The soft tissues are present in the region delimited between the brown line and white line. The fracture is indicated by the black dotted line. The parameters values t_j and ε_{r_j} used in Eq. (6) are shown in column named "Ovine" in Table 1, which compute to $\varepsilon_{r_{av}} = 20.19$. The other parameters are $B = 3$, $Q = 3$ and $g = 2$ for the central region of the bone and $g = 3$ for the edge regions. It is possible to identify the presence of the fracture in both planes represented in Fig. 19 (a), by its strong response. The quantitative metric gives SCR = 6.6 dB in this case, indicating good detection.

D. TRANSVERSAL FRACTURE IN GOAT LEG WITH ALL TISSUES

In this test we used an *ex-vivo* leg from a goat with all the tissues, including skin and fur. This is very close to a clinical scenario for testing our concept.

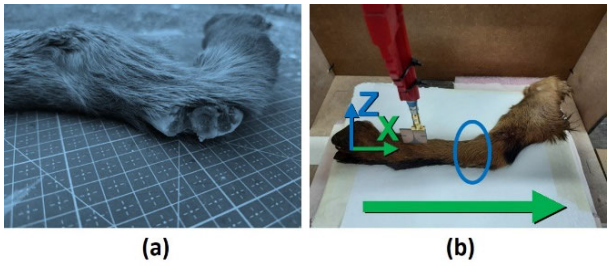

FIGURE 20. Experimental setup (a) caprine tibia cut preserving soft tissue, (b) caprine leg with transversal fracture.

The antenna positioning was the same as described for the ovine leg fracture. The tibia was carefully sectioned, preserving tendon, nerves, and skin in the scanning area, as shown in Fig. 20 (a). The fractured leg was positioned and aligned in the setup, with the skin incision at the opposite side of the scanning area, Fig. 19 (b).

The reconstructed image of the fractured leg is shown in Fig. 21 in two planes. The bone region is delimited by the

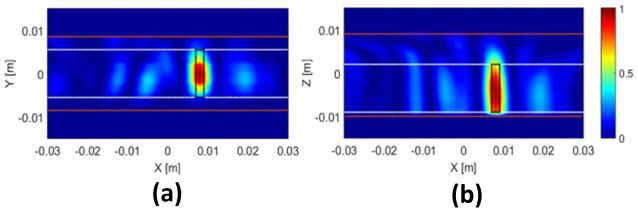

FIGURE 21. Reconstructed images from *ex-vivo* caprine leg (a) at the slice at $z = -4$ *mm*, (b) at the slice at $y = 0$ *mm*, with $\varepsilon_{r_{av}} = 20.07$. The white lines define the bone boundary, and the brown lines the soft tissues boundary.

white lines, while the soft tissues are present in the regions between the brown and white lines. The fracture is indicated by the black dotted line. The parameters values t_j and ε_{r_j} used in Eq. (6) are shown in the column named "Goat" in Table 1 which compute to $\varepsilon_{r_{av}} = 20.07$. $B = 3$, $Q = 3$ and $g = 2$ for the central region of the bone and $g = 3$ for the edge regions. The fracture is clearly detected in the correct location, with SCR = 7.8 dB.

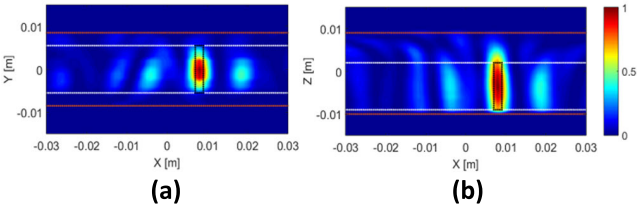

FIGURE 22. Reconstructed images from *ex-vivo* caprine leg (a) at the slice at $z = -4$ *mm*, (b) at the slice at y = 0 mm, with $\varepsilon_{r_{av}} = +20\%$. The white lines define the bone boundary, and the brown lines the soft tissues boundary.

We also instigated the impact that the uncertainty in the estimation of the average permittivity has on the image reconstruction, given the uncertainty of the different tissue thicknesses and dielectric constants involved in the calculation. For that, we repeated the image reconstruction for this leg example, with different average permittivity values ranging in the -20% to $+20\%$ interval with respect to nominal. The SCR remains almost unchanged within the $\pm 10\%$ interval, while it reduces by 1.4 dB for $\pm 20\%$ deviation with respect to nominal, *i.e.*, $\varepsilon_{r_{av}} = 16$ and $\varepsilon_{r_{av}} = 24$. We present in Fig. 22 the result for the latter, corresponding to SCR = 6.4 dB. The degradation of the SCR comes from a slight increase in the artifact level away from the fracture location. However, it is still a clear detection, in the correct location, with an SCR above a minimum of 3 dB.

This experimental result reinforces that the method is robust enough to cope with the uncertainties that are expected in practical real-life applications, with actual biologic limbs. It is stressed that the image quality obtained for this air-operated system, without using any contact liquid, is made possible by the developed very robust image inversion algorithm, which evolved from [8]. Table 3 shows the comparison between our proposed MWI system to detect bone fractures with existing ones.

TABLE 3. Comparison of the state of the art on bone microwave imaging with our work.

REF	ARTIFACT REMOVE	OBJECTIVE	CONFIGURATION	PHANTOM	COMMENT
[11]	Rotation subtraction	Detecting longitudinal lesions bone	**Two antennas** are used in the scan (s11 and s21 responses)	**Regular boundary tubes** representing the cortical bone, bone marrow, and a lesion; Longitudinal lesion (**radius of 4 mm and extension of 130 mm**)	**Lesions** are **quite large** The MWI system is **fixed**, bulky and expensive Image quantification: signal to clutter ratio
[16]	Adaptative SVD	Detecting transversal bone fractures	A **single antenna** is used in radar mode (s11 response)	**Realistic phantom** composed of **animal** bone and skin with **irregular boundary with 1mm thickness**	The MWI system is **fixed** and bulky Image quantification: signal to clutter ratio
[12]	Rotation subtraction	Detecting longitudinal lesions bone	**Two antennas** are used in the scan (s11 and s21 responses)	**Regular boundary tubes** representing the cortical bone, and a lesion Longitudinal lesion **with extension of 7.5 cm** and **radius of 1 cm and 4 cm**, respectively	**Lesions** are **quite large** The MWI system is **fixed**, bulky and expensive Image quantification: signal to clutter ratio
THIS WORK	Adaptative SVD	Detecting transversal, oblique and multiples bone fractures	A **single antenna** is used in radar mode (s11 response)	**Realistic phantom** composed of **animal** bones and integral **animal leg with fracture thickness 1 mm. Double fracture with 15mm between them.** Resolution $\lambda/2 = 15$mm.	The MWI system is **portable** and **compact** Image quantification: signal to clutter ratio

V. CONCLUSION

This study demonstrates the feasibility of detection of thin arbitrarily oriented fractures in superficial bones like the tibia, using a portable, compact, low complexity, and contactless MWI system. This required the generalization for 3D geometry of our previous inverse scattering formulation, which involved only 2D measurement data taken in a single linear scan.

Furthermore, the work evolved from tests on ideal cylindrical shape phantoms, or on stripped bones, now to complete ovine and caprine legs, with all the involved natural tissues, including skin and fur. The used cylindrical grid scan reinforced the detection and location of the bone fractures, providing information on its depth and shape.

Our image reconstruction algorithm detected all the tested fractures, with high SCR quality metric values even with the fully preserved tissues, without the need for considering previous knowledge of the phantom shape, or severe leg positioning restrictions. We accessed the system resolution showing that it approaches the theoretical limit. We also demonstrated good robustness of the method to permittivity and tissue thickness estimation uncertainty, and to slight involuntary movement of the patient during the exam, which certainly occur in practical clinical cases.

The obtained results prove the interest and feasibility of our method for positive fracture detection in superficial bones in very close to pre-clinical use cases, and the feasibility of using a quite simple portable and inexpensive examination setup. This contributes to making this imaging modality accessible for first response screening in ambulances, retirement houses, school infirmary, in low-income settings, and veterinary clinics.

ACKNOWLEDGMENT

The authors would like to thank C. Brito for fabrication of the antenna and Prof. Erik Farias da Silva from IFPB for assistance with the measurements.

REFERENCES

[1] J. B. Hobbs, N. Goldstein, K. E. Lind, D. Elder, G. D. Dodd, and J. P. Borgstede, "Physician knowledge of radiation exposure and risk in medical imaging," *J. Amer. College Radiol.*, vol. 15, no. 1, pp. 34–43, Jan. 2018.

[2] E. J. Bond, X. Li, S. C. Hagness, and B. D. V. Veen, "Microwave imaging via space-time beamforming for early detection of breast cancer," *IEEE Trans. Antennas Propag.*, vol. 51, no. 8, pp. 1690–1705, Aug. 2003.

[3] D. Byrne, M. Sarafianou, and I. J. Craddock, "Compound radar approach for breast imaging," *IEEE Trans. Biomed. Eng.*, vol. 64, no. 1, pp. 40–51, Jan. 2017.

[4] J. M. Felício, J. M. Bioucas-Dias, J. R. Costa, and C. A. Fernandes, "Microwave breast imaging using a dry setup," *IEEE Trans. Comput. Imag.*, vol. 6, pp. 167–180, 2020.

[5] B. J. Mohammed, A. M. Abbosh, S. Mustafa, and D. Ireland, "Microwave system for head imaging," *IEEE Trans. Instrum. Meas.*, vol. 63, no. 1, pp. 117–123, Jan. 2014.

[6] A. T. Mobashsher, A. M. Abbosh, and Y. Wang, "Microwave system to detect traumatic brain injuries using compact unidirectional antenna and wideband transceiver with verification on realistic head phantom," *IEEE Trans. Microw. Theory Techn.*, vol. 62, no. 9, pp. 1826–1836, Sep. 2014.

[7] J. A. T. Vasquez, R. Scapaticci, G. Turvani, G. Bellizzi, D. O. Rodriguez-Duarte, N. Joachimowicz, B. Duchêne, E. Tedeschi, M. R. Casu, L. Crocco, and F. Vipiana, "A prototype microwave system for 3D brain stroke imaging," *Sensors*, vol. 20, no. 9, p. 2607, May 2020.

[8] M. T. Islam, M. Z. Mahmud, M. T. Islam, S. Kibria, and M. Samsuzzaman, "A low cost and portable microwave imaging system for breast tumor detection using UWB directional antenna array," *Sci. Rep.*, vol. 9, no. 1, pp. 1–13, Oct. 2019.

[9] Micrima-Maria Update. *Micrima Enters Into Distribution Agreement With Hologic for Its Novel Breast Imaging System MARIA*. Accessed: Mar. 2023. [Online]. Available: https://www.micrima.com/about-us

[10] G. Ruvio, A. Cuccaro, R. Solimene, A. Brancaccio, B. Basile, and M. J. Ammann, "Microwave bone imaging: A preliminary scanning system for proof-of-concept," *Healthcare Technol. Lett.*, vol. 3, no. 3, pp. 218–221, Sep. 2016.

[11] B. Khalesi, B. Sohani, N. Ghavami, M. Ghavami, S. Dudley, and G. Tiberi, "Free-space operating microwave imaging device for bone lesion detection: A phantom investigation," *IEEE Antennas Wireless Propag. Lett.*, vol. 19, no. 12, pp. 2393–2397, Dec. 2020.
[12] B. Khalid, B. Khalesi, N. Ghavami, L. Sani, A. Vispa, M. Badia, S. Dudley, M. Ghavami, and G. Tiberi, "3D Huygens principle based microwave imaging through MammoWave device: Validation through phantoms," *IEEE Access*, vol. 10, pp. 106770–106780, 2022.
[13] A. Vispa, L. Sani, M. Paoli, A. Bigotti, G. Raspa, N. Ghavami, S. Caschera, M. Ghavami, M. Duranti, and G. Tiberi, "UWB device for breast microwave imaging: Phantom and clinical validations," *Measurement*, vol. 146, pp. 582–589, Nov. 2019.
[14] K. S. Sultan, B. Mohammed, M. Manoufali, and A. M. Abbosh, "Portable electromagnetic knee imaging system," *IEEE Trans. Antennas Propag.*, vol. 69, no. 10, pp. 6824–6837, Oct. 2021.
[15] K. S. Sultan, B. Mohammed, M. Manoufali, A. Mahmoud, P. C. Mills, and A. Abbosh, "Feasibility of electromagnetic knee imaging verified on ex-vivo pig knees," *IEEE Trans. Biomed. Eng.*, vol. 69, no. 5, pp. 1651–1662, May 2022.
[16] K. C. Santos, C. A. Fernandes, and J. R. Costa, "Feasibility of bone fracture detection using microwave imaging," *IEEE Open J. Antennas Propag.*, vol. 3, pp. 836–847, 2022.
[17] K. C. Santos, C. A. Fernandes, and J. R. Costa, "Experimental evaluation of thin bone fracture detection using microwave imaging," in *Proc. 16th Eur. Conf. Antennas Propag. (EuCAP)*, Madrid, Spain, Mar./Apr. 2022, pp. 1–3.
[18] X. Li and S. C. Hagness, "A confocal microwave imaging algorithm for breast cancer detection," *IEEE Microw. Wireless Compon. Lett.*, vol. 11, no. 3, pp. 130–132, Mar. 2001.
[19] M. A. Elahi, M. Glavin, E. Jones, and M. O'Halloran, "Artifact removal algorithms for microwave imaging of the breast," *Prog. Electromagn. Res.*, vol. 141, pp. 185–200, 2013.
[20] E. Ricci, S. di Domenico, E. Cianca, T. Rossi, and M. Diomedi, "PCA-based artifact removal algorithm for stroke detection using UWB radar imaging," *Med. Biol. Eng. Comput.*, vol. 55, no. 6, pp. 909–921, Jun. 2017.
[21] F. Abujarad, A. Jostingmeier, and A. S. Omar, "Clutter removal for landmine using different signal processing techniques," in *Proc. 10th Int. Conf. Grounds Penetrating Radar (GPR)*, Jun. 2004, pp. 697–700.
[22] P. K. Verma, A. N. Gaikwad, D. Singh, and M. J. Nigam, "Analysis of clutter reduction techniques for through wall imaging in UWB range," *Prog. Electromagn. Res. B*, vol. 17, pp. 29–48, 2009.
[23] G. Ruvio, R. Solimene, A. Cuccaro, D. Gaetano, J. E. Browne, and M. J. Ammann, "Breast cancer detection using interferometric MUSIC: Experimental and numerical assessment," *Med. Phys.*, vol. 41, no. 10, Oct. 2014, Art. no. 103101.
[24] J. M. Lopez-Sanchez and J. Fortuny-Guasch, "3-D radar imaging using range migration techniques," *IEEE Trans. Antennas Propag.*, vol. 48, no. 5, pp. 728–737, May 2000.
[25] S. Gabriel, R. W. Lau, and C. Gabriel, "The dielectric properties of biological tissues: III. Parametric models for the dielectric spectrum of tissues," *Phys. Med. Biol.*, vol. 41, no. 11, pp. 2271–2293, Nov. 1996.
[26] A. C. Pelicano and R. C. Conceição, "Development of a 3D anthropomorphic phantom generator for microwave imaging applications of the head and neck region," *Sensors*, vol. 20, no. 7, p. 2029, Apr. 2020.
[27] C. Dachena, A. Fedeli, A. Fanti, M. B. Lodi, G. Fumera, A. Randazzo, and M. Pastorino, "Microwave imaging of the neck by means of artificial neural networks for tumor detection," *IEEE Open J. Antennas Propag.*, vol. 2, pp. 1044–1056, 2021.
[28] (May 2022). *CST-Computer Simulation Technology*. Accessed: May 2022. [Online]. Available: https://www.cst.com/
[29] N. Ghavami, G. Tiberi, D. J. Edwards, and A. Monorchio, "UWB microwave imaging of objects with canonical shape," *IEEE Trans. Antennas Propag.*, vol. 60, no. 1, pp. 231–239, Jan. 2012.
[30] L. Sani, N. Ghavami, A. Vispa, M. Paoli, G. Raspa, M. Ghavami, F. Sacchetti, E. Vannini, S. Ercolani, A. Saracini, M. Duranti, and G. Tiberi, "Novel microwave apparatus for breast lesions detection: Preliminary clinical results," *Biomed. Signal Process. Control*, vol. 52, pp. 257–263, Jul. 2019.
[31] S. Mukherjee, L. Udpa, S. Udpa, E. J. Rothwell, and Y. Deng, "A time reversal-based microwave imaging system for detection of breast tumors," *IEEE Trans. Microw. Theory Techn.*, vol. 67, no. 5, pp. 2062–2075, May 2019.
[32] R. Benny, T. A. Anjit, and P. Mythili, "An overview of microwave imaging for breast tumor detection," *Prog. Electromagn. Res. B*, vol. 87, pp. 61–91, 2020.
[33] B. Khalesi, B. Khalid, N. Ghavami, G. Raspa, M. Ghavami, S. Dudley-McEvoy, and G. Tiberi, "A microwave imaging procedure for lung lesion detection: Preliminary results on multilayer phantoms," *Electronics*, vol. 11, no. 13, pp. 2105–2115, Jul. 2022.

KESIA C. SANTOS (Student Member, IEEE) was born in João Pessoa, Brazil, in 1981. She received the Technologist degree in telecommunications from the Federal Institute of Paraíba (IFPB), João Pessoa, in 2004, after completing a three-year education program, and the M.S.E.E. degree from the Federal University of Rio Grande do Norte, Natal, Brazil, in 2005. She is currently pursuing the Ph.D. degree with Instituto Superior Técnico (IST), Lisbon, Portugal.

Since 2010, she has been a Professor of electronics and antennas with IFPB. Her main research interests include microwave imaging, biomedical solutions for low-income populations, the design and development of antennas, and encouragement actions to bring more girls to engineering.

CARLOS A. FERNANDES (Life Senior Member, IEEE) received the Licenciado, M.Sc., and Ph.D. degrees in electrical and computer engineering from Instituto Superior Técnico (IST), Technical University of Lisbon, Lisbon, Portugal, in 1980, 1985, and 1990, respectively.

In 1980, he joined IST, where he is currently a Full Professor with the Department of Electrical and Computer Engineering in the areas of microwaves, radio wave propagation, and antennas. He is also a Senior Researcher with Instituto de Telecomunicacões, Lisbon, and a member of the Board of Directors. He has coauthored a book, two book chapters, and more than 200 technical papers in peer-reviewed international journals and conference proceedings. He holds seven patents in the areas of antennas and radiowave propagation modeling. His current research interests include dielectric antennas for millimeter wave applications, antennas, and propagation modeling for personal communication systems, RFID and UWB antennas, artificial dielectrics, and metamaterials.

Dr. Fernandes was the Guest Editor of the Special Issue on Antennas and Propagation at mm- and Sub mm-Waves, from the IEEE Transactions on Antennas and Propagation, in April 2013.

JORGE R. COSTA (Senior Member, IEEE) was born in Lisbon, Portugal, in 1974. He received the Licenciado and Ph.D. degrees in electrical and computer engineering from Instituto Superior Técnico (IST), Technical University of Lisbon, Lisbon, in 1997 and 2002, respectively.

He is currently a Senior Researcher with Instituto de Telecomunicações, Lisbon. He is also a Full Professor with Departamento de Ciências e Tecnologias da Informação, Instituto Universitário de Lisboa (ISCTE-IUL). He is the coauthor of four patent applications and more than 200 contributions to peer-reviewed journals and international conference proceedings. More than 50 articles have appeared in IEEE journals. His current research interests include lenses, transmit arrays, and biomedical antennas.

Dr. Costa was the Co-Chair of the Technical Program Committee of the European Conference on Antennas and Propagation (EuCAP 2015), Lisbon, and the General Vice-Chair of EuCAP 2017, Paris, EuCAP 2020, online and EuCAP 2021, Madrid. He served as an Associate Editor for the IEEE Transactions on Antennas and Propagation, from 2010 to 2016. He was the Guest Editor of the IEEE Transactions on Antennas and Propagation Special Issue on Antennas and Propagation at mm- and sub mm-Waves, in 2013. He is also an Associate Editor of the IEEE Open Journal of Antennas and Propagation.